Terahertz parametric generators and detectors for nondestructive testing through high-attenuation packaging materials

Kosuke Murate, *Member, IEEE*, Sota Mine, and Kodo Kawase

Abstract— **Here, we introduce an injection-seeded terahertz (THz)-wave parametric generator (is-TPG) spectroscopic system and its application to nondestructive inspection through a packaging material with high attenuation. Recent technological innovations have dramatically improved is-TPG output. Combined with THz parametric detection, whereby detection is performed in the reverse process of generation, a spectrometer with an extremely high dynamic range has been achieved. THz spectroscopic imaging has enabled the previously difficult visualization of substance spatial distributions, even through thick packaging materials. Moreover, the introduction of machine learning has improved the accuracy of identification. High-speed wavelength tuning and multi-wavelength generation enable real-time acquisition of sample information and real-time identification by image recognition, thus broadening the range of applicability of the is-TPG. Additionally, detection sensitivity has improved to a level of < 1 aJ through multi-stage THz parametric detection. The system combining is-TPG and THz parametric detection now exhibits a dynamic range of 125 dB, enabling imaging through thick, high scattering materials with an attenuation factor of −100 dB; to our knowledge, such measurements are difficult to achieve with other THz-wave systems.**

Index Terms— **Terahertz wave parametric generator, Terahertz radiation, Nondestructive testing, Nonlinear optics, Machine learning.**

Manuscript received XXX XX, 2023; revised XXX XX, 2023; accepted XXX XX, 2023. Date of publication XXX XX, 2023; date of current version XXX XX, 2023. This work was partially supported by JST FOREST Program (JPMJFR212J); Japan Society for the Promotion of Science KAKENHI (19H02627, 22H00212); Foundation of Public Interest of Tatematsu, Konica Minolta Science and Technology Foundation, and The Naito Science & Engineering Foundation. (Corresponding author: Kosuke Murate)

K. Murate, S. Mine, and K. Kawase are with the Department of Electronics, Graduate school of Engineering, Nagoya University, Furocho, Chikusa, Nagoya, 4648603, Japan (e-mail: murate@nuee.nagoya-u.ac.jp, mine.sota.e8@s.mail.nagoya-u.ac.jp, kodo@nagoya-u.jp).

I. INTRODUCTION

The expected applications of terahertz (THz) waves include nondestructive testing through packaging materials. Specifically, 1–2 THz is the region where chemical compounds show fingerprint spectra while retaining moderate transmittance through typical packaging materials such as paper, fabrics, plastics, and leather. Spectra in the THz range are associated with characteristics such as molecular rotation, vibrational motion, and phonon modes, contributing to the identification of samples (e.g., illicit drugs, explosives, and pharmaceuticals) and familiar items (e.g., sugars, amino acids, and vitamins) [1–9]. Moreover, there is increasing demand for THz-wave nondestructive testing through packaging materials; applications include illicit drug testing at customs, prescription drug testing at hospitals, quality control at factories, and inspection of explosives and other hazardous materials at various gates [10–12]. Although shield-mediated THz spectroscopy system-based imaging and spectroscopic identification have been described [13–16], time-domain spectroscopy is often inappropriate for practical applications because of the inevitable packaging material related effects of strong absorption, multiple reflections, and scattering. Thus, for practical applications, spectroscopy with a widely tunable THz source is preferred to overcome the effects of packaging materials.

Among the many THz-wave generation techniques, the development of THz parametric sources has been pursued as a widely tunable and coherent source. Around the year 1970, researchers from Stanford University reported the first successful attempt at THz parametric generation [17, 18]. Although they achieved higher conversion efficiency than had been reported via difference frequency generation, the extraction efficiency of THz-waves from the $LiNbO_3$ crystal was poor because the crystal absorbed THz-waves; thus, sufficient output was not obtained. Accordingly, this technology was forgotten for many years. However, an efficient extraction method that involved introducing a monolithic grating coupler to a THz-wave parametric oscillator (TPO) was reported in the 1990s [19]. During the 2000s, an injection-seeded THz-wave parametric generator (is-TPG) was developed [20]; this system does not require a resonator structure to generate intense THz-waves. In the 2010s, a microchip Nd:YAG laser [21] was introduced as a pumping source for the is-TPG, leading to a significant increase in output power [22]. The use of microchip lasers has also facilitated increases in is-TPG output power, along with technological innovations such as multi-wavelength generation [23] and parametric detection/amplification [24–27]. There have been numerous developments in THz parametric generation/detection, such as compact backward oscillators involving a quasi-phase-matching crystal [28–30], generation/detection at > 5 THz using a KTP crystal [31, 32], a THz-wave parametric oscillator using THz-wave resonance inside a thin crystal [33], an intracavity-type THz-wave parametric oscillator [33, 35], a parametric source involving a high repetition rate laser [35, 37], achievement of high power by the pulsed injection seed beam [38], achievement of high efficiency through a cascade process [39], and parametric detection using a femtosecond pump laser [40]. Concurrently, extensive theoretical studies have validated the operating and optimization principles of THz parametric generation and detection [41, 42].

An is-TPG involving an MgO:LiNbO$_3$ crystal (i.e., the LiNbO$_3$ crystal) has demonstrated high peak power output, Fourier limit linewidth, and wide tunability that includes the bandwidth important for nondestructive testing [43]. Because this approach also allows ultra-sensitive THz-wave detection [25], it is appropriate for nondestructive testing applications over highly attenuated packaging materials with high scattering properties. In this paper, we describe the development and recent evolution of microchip Nd:YAG laser-pumped is-TPG systems and THz parametric detection, along with progress in nondestructive testing techniques that use this technology.

II. THz PARAMETRIC GENERATION AND DETECTION

When an intense laser beam pumps a nonlinear optical crystal, a near-infrared (NIR) beam (Stokes or idler beam) and a THz-wave (signal beam) are generated. These phenomena are caused by polariton-related stimulated Raman scattering, which results from coupling between the phonons and the THz-wave [44, 45]. Stimulated Raman scattering is observed in polar crystals such as LiNbO$_3$, LiTaO$_3$, and GaP. Among these examples [46, 47], LiNbO$_3$ crystals are most appropriate for use in an is-TPG because they are transparent over the visible-to-NIR range and have a high damage threshold, along with a high parametric gain. In THz parametric generation, the energy conservation law $\omega_p = \omega_s + \omega_t$ and the momentum conservation law $k_p = k_s + k_t$ are satisfied among the pump beam (ω_p), the Stokes (idler) beam (ω_s), and the THz-wave (ω_t). The Stokes beam and THz-wave are generated at angles that satisfy the non-collinear phase-matching condition. However, as shown in Fig. 1(a), broadband and weak THz-waves are generated when only the pump beam is incident on the crystal; this phenomenon is referred to as THz-wave parametric generation (TPG).

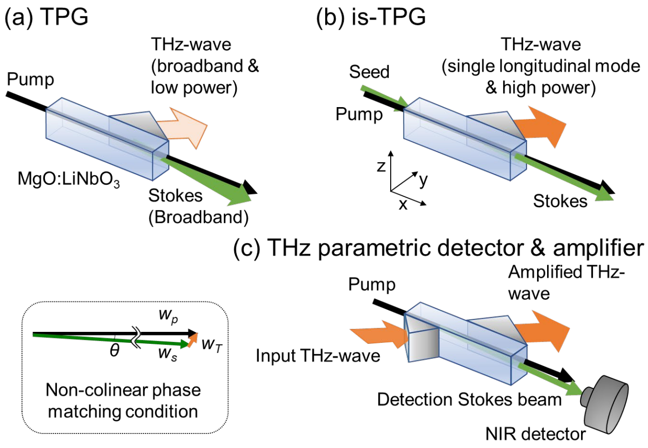

Fig. 1. (a) Terahertz (THz) parametric generation (TPG), (b) injection-seeded THz parametric generation (is-TPG), and (c) THz parametric detection and amplification. NIR: near-infrared.

In contrast, as shown in Fig. 1(b), TPG with external injection seeding to the Stokes beam is called an injection-seeded THz-wave parametric generator (is-TPG). When the wavelength and angle of the seed beam satisfy the non-collinear phase-matching condition, only the Stokes beam of identical wavelength is amplified; the THz-wave generated in conjunction with the Stokes beam becomes narrower and more powerful [43]. Notably, the pump beam, seed beam, and THz-wave are all single longitudinal modes. When the wavelength and angle of the injected seed beam are controlled, the THz wavelength can also be controlled; this control results in wide tunability. A 4f achromatic optical system, comprising a diffraction grating and two lenses, has been the most commonly used system for automatic control of the angle of the injected seed beam [48]. In this optical system, the incident angle is altered by the diffraction grating in accordance with changes in seed wavelength; the phase-matching angle is automatically approximately satisfied. The tuning range of the is-TPG is mainly limited by the reduction in parametric gain on the low-frequency side and by crystal absorption loss on the high-frequency side. The low-frequency side is improved by increasing the pump beam intensity and diameter, whereas the high-frequency side is improved by shallow total reflection of the pump beam at the THz-wave exit y-surface of the crystal; these changes result in wide tunability from 0.4 to 5 THz [49, 50].

Next, we discuss the pump laser for the is-TPG. When the is-TPG was first developed, a single longitudinal mode Nd:YAG laser with a pulse width of approximately 15 ns was used as the pump [20]. However, at that pulse width, the gain of stimulated Brillouin scattering was approximately 1000-fold larger than the gain of stimulated Raman scattering in a LiNbO$_3$ crystal; this difference led to the substantial reduction of THz-wave generation efficiency [51]. The conversion efficiency was measured as a function of the pump pulse width. A conversion efficiency of approximately 10^{-7} was obtained with a pulse width of 15 ns; however, a conversion efficiency of approximately 10^{-4}, which is near the Manley–Rowe limit, was achieved in the region of several hundred ps or less, where stimulated Brillouin scattering (which reaches a steady state in approximately 1.5 ns) does not affect conversion efficiency. Notably, if the pulse width becomes insufficient, the linewidth increases and the brightness of the THz-wave decreases because of the Fourier limit. Therefore, the introduction of a single-longitudinal-mode microchip Nd:YAG laser, which provides an intense pump pulse with an approximately 500-ps pulse width, has enabled the generation of high-brightness THz-waves with a narrow linewidth; this approach involves maximizing the gain in stimulated Raman scattering (i.e., induced polariton scattering) while suppressing stimulated Brillouin scattering. With the introduction of this laser and its amplification technology, peak THz-wave output has reached approximately 100 kW [22], whereas the previous output was approximately 300 mW. Additionally, the microchip Nd:YAG laser is a tiny laser that integrates the cavity and laser medium, thus contributing to miniaturization of the entire experimental system. Furthermore, semiconductor laser pumping and passive Q-switching of the microchip Nd:YAG laser have advantages over conventional flashlamp-pumped Nd:YAG lasers, such as high stability.

THz-wave parametric detection [24] and amplification [26] can also be achieved as shown in Fig. 1(c), using THz-waves as an injection seed. The TPG-generated broadband Stokes beam is narrowed and increased in power (this comprises the detection Stokes beam); the injected THz-wave is amplified. In this context, the observation of the detection Stokes beam constitutes the THz-wave parametric detection method, whereby THz-waves are upconverted to an NIR beam using the inverse process of the is-TPG. This method allows the use of highly sensitive NIR detectors such as pyroelectric detectors, photodetectors, and image sensors for the detection Stokes beam; moreover, the high parametric gain of the $LiNbO_3$ crystal can be utilized on the detection side. Accordingly, THz parametric detection can be conducted at room temperature with sensitivity that is several orders of magnitude higher than the sensitivity achieved during direct detection of THz-waves with a cryogenic Si bolometer. Additionally, although the non-collinear phase-matching condition must be satisfied similar to the generation method, the THz-wave incident angle tolerance on the detection side is large because the THz wavelength is much longer than the wavelength of the pump beam, and the detection area is wide; thus, it is highly practical. The THz wavelength can be identified from the generation angle of the detection Stokes beam. Therefore, image sensor-mediated observation of the detection Stokes beam allows simultaneous measurement of the wavelength and intensity of the THz-wave; these characteristics are also highly practical.

III. SPECTROSCOPIC MEASUREMENT SYSTEM USING IS-TPG

Figure 2 shows the developed THz spectroscopic system that comprises an is-TPG and a THz parametric detector [52]. The pump beam from a microchip Nd:YAG laser is amplified to approximately 20 mJ by a Nd:YAG amplifier. The amplified beam is then split by a beam splitter into two parts for THz-wave generation and detection; it is subsequently injected into each $LiNbO_3$ crystal. The main injection seeding source is a continuous-wave external cavity laser diode (ECLD), which is injected into the crystal through achromatic optical setup after its intensity has been increased to several hundred mW with an optical amplifier. The THz-wave generated by the $LiNbO_3$ crystal is transmitted through the sample, upconverted to a detection Stokes beam by the detection crystal, and then observed using an NIR detector. Because the position of the detection Stokes beam changes according to THz wavelength as described above, it can be measured with a pyroelectric detector on an automated linear stage.

An example of the power spectrum obtained by this system is shown in the inset of Fig. 2. Because THz parametric detection is a nonlinear process, the intensity of the detection Stokes beam does not vary in a linear manner according to incident THz-wave intensity. Thus, the dynamic range of the THz-wave cannot be directly determined from the range of the detection Stokes beam. Here, an attenuator is inserted into the optical path of the THz-wave; the power spectrum is measured at each attenuation level, and the dynamic range is obtained from the attenuation level that reaches the noise level. In the example shown in the inset of Fig. 2, the maximum dynamic range is > 80 dB. Note that the maximum dynamic range of the experimentally confirmed is-TPG generation/detection system is 125 dB, as described below [25]. Compared with THz–time-domain spectroscopy, the positional tolerance of the THz-wave incident on the $LiNbO_3$ crystal (Si prism) of the detector is on the millimeter scale, and the frequency information of the THz-wave can be directly measured without Fourier transform; thus, it is appropriate for spectroscopic measurements through thick packaging materials where multiple reflections and scattering occur. Indeed, we have reported imaging of the spatial distribution of saccharides through multi-layered thick packaging materials (e.g., cardboard, bubble wrap, and thick envelopes) that exhibited attenuation rates greater than −60 dB [53], along with three-dimensional computed tomography imaging of hard plastic products that exhibited high attenuation [54].

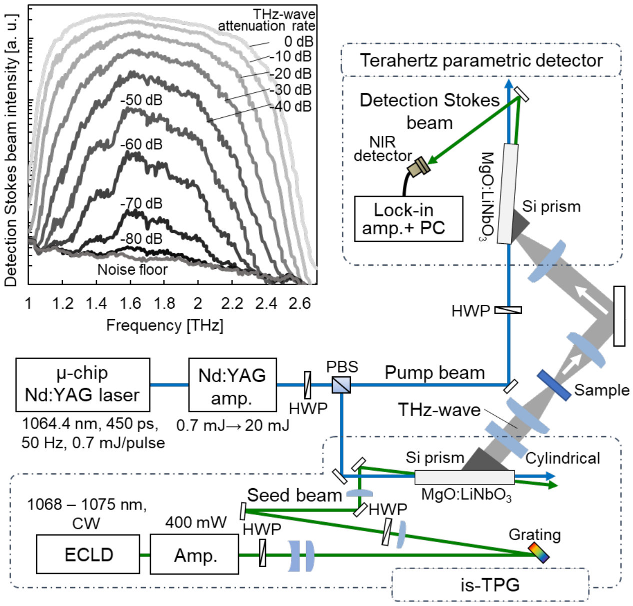

Fig. 2. Spectroscopy system combining is-TPG and THz parametric detector. Upper left inset shows representative power spectrum and dynamic range measurements. CW: continuous wave; ECLD: external cavity laser diode; HWP: half-wave plate; PBS: polarizing beam splitter.

IV. CHEMICAL COMPOUNDS IDENTIFICATION WITH MACHINE LEARNING

Although is-TPG measurement systems have demonstrated sufficient performance, as discussed above, analysis methods for sample identification require further improvement. A previous study used a identification method based on simple regression analysis with matrix operations [11, 53]. Although this method exhibited high accuracy for discriminating samples under specific packaging materials that were assumed in advance, it was insufficient for unknown packaging materials or noisy data. Real-world applications require the ability to discriminate samples hidden by diverse packaging materials.

In this study, we introduced machine learning analysis for is-TPG measurements to detect and identify hidden samples. The method we used in previous studies [11, 53] also constitutes a type of machine learning; however, identification thresholds must be established. Thus, these earlier attempts are distinct from the methods proposed here.

Machine learning is widely used for material identification and quantitative testing; it is also attracting attention as a method for sample identification via THz spectroscopy [55–61]. However, the identification usually involves a sample or barrier material for which the algorithm has already received training. In this study, we developed a versatile system that can discriminate saccharides through various packaging materials using is-TPG spectroscopy with machine learning methods [62].

The experimental system is equivalent to the system shown in Fig. 2, but the methods for sample processing and data management differ. The machine learning algorithms learn patterns by analyzing large amounts of data. We measured samples of three sugars (maltose, glucose, and lactose) that were masked by several packaging materials with different attenuation rates; we obtained a total of 852 spectra. After training the machine with a large number of spectra, which exhibited low-to-high attenuation, we could discriminate among samples concealed by unknown packaging materials. We compared the discrimination accuracies of three machine learning methods: support vector machine [63, 64], k-nearest neighbor [65], and random forest [66]. These methods are widely used for easy classification; see References for more information.

The saccharides identification results through the trained and untrained packaging materials are shown in the upper and lower parts of Table 1, respectively. Through the trained packaging materials, all methods identified the saccharides with nearly 100% accuracy. Thus, we confirmed that the spectroscopic system could discriminate saccharides through the trained packaging materials. Through the low-attenuation untrained packaging materials, all learning methods achieved 100% accuracy. Through the high-attenuation untrained packaging materials, the support vector machine, k-nearest neighbor, and random forest algorithms achieved respective accuracies of 88.9%, 77.8%, and 80.0%. Although the spectra obtained through the high-attenuation packaging materials were near the noise level and the original spectral shape was not maintained as shown in Fig. 4(a), an accuracy of 88.9% was achieved; this representative result demonstrated the advantages of machine learning. Furthermore, a single system could discriminate samples, even with > 2 unknown types of packaging materials that had significantly different attenuation rates; this finding confirms the versatility of the system. Thus, machine learning techniques are expected to significantly contribute to the development of future applications. Additionally, although the optimal method may vary according to the training data quantity, learning conditions, and other factors, the support vector machine method was effective under the conditions of the present study.

TABLE I
DISCRIMINATION ACCURACY FOR VARIOUS SAMPLES.

Packaging materials name		Machine learning method		
		SVM	KNN	RF
Trained packaging materials (Mean of 5 kinds of shielding)		98.7%	96.9%	98.2%
Untrained packaging materials	Low-attenuation materials model (-10 dB)	100%	100%	100%
	High-attenuation materials model (-65 dB)	88.9%	77.8%	80.0%

SVM: support vector machine; kNN: k-nearest neighbor; RF: random forest.

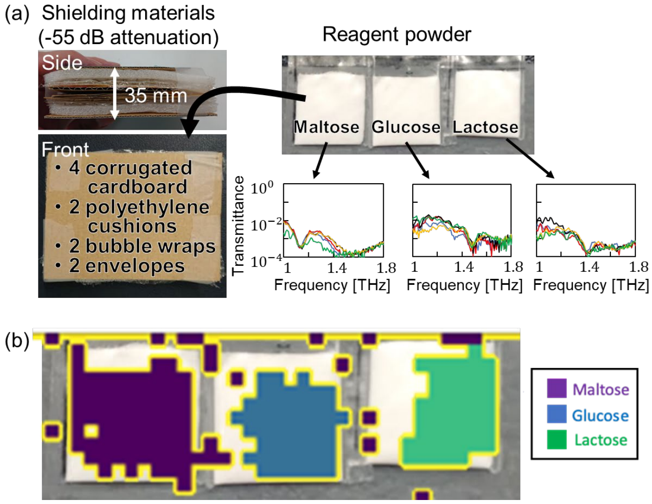

Fig. 3. (a) Packaging materials and saccharide samples used for spectroscopic imaging measurements. Saccharides were sandwiched between four types of packaging materials that attenuated the THz-wave to −65 dB at 1.5 THz. (b) Spatial distributions of saccharides identified by machine learning.

Next, spectroscopic imaging was performed using the proposed system. A sample concealed by high-attenuation packaging materials, as shown in Fig. 3(a), was placed at the THz focal point and raster-scanned using an X-Y stage with a spatial resolution of approximately 1 mm. Seven frequencies were used, all of which had the highest contribution ratios according to random forest analysis. Preliminary analyses confirmed that the accuracy was only degraded by a few percent, even with seven frequencies. The spectrum at each point was identified by support vector machine analysis. The results were displayed as individual pixel values, then superimposed on a photograph of the sample, as shown in Fig. 3(b). The saccharides distribution could be visualized, even through packaging materials with higher attenuation than previously attempted.

V. HIGH-SPEED SPECTROSCOPY USING AN IS-TPG

The is-TPG-based spectroscopic measurement method is described above. Because the is-TPG is a tunable source, the measurement time necessary for spectroscopy analysis was problematic. The measurement time can be significantly reduced if the THz wavelength can be tuned at a high speed; thus, we explored techniques to enable high-speed tuning of the injection seed. A commercially available ECLD, used as a seed source in conventional is-TPG, is incapable of rapidly changes in wavelength. High-speed spectroscopy involving a vertical-cavity surface-emitting laser as a seed source has also been reported [67], but discrete wavelength switching is difficult.

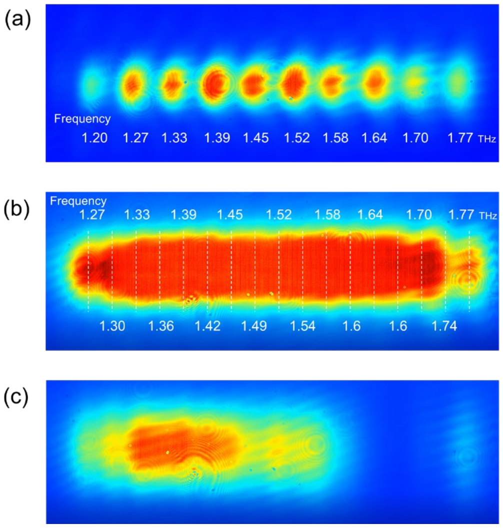

Fig. 4. Detection Stokes beams when (a) 10 wavelengths were switched from 1.20 THz to 1.77 THz, (b) 17 wavelengths were switched from 1.27 THz to 1.77 THz, and (c) maltose was inserted into the THz path during switching among 17 wavelengths.

Therefore, we developed an ECLD with a digital micromirror device (DMD) as a wavelength selection mechanism [68, 69] to construct an is-TPG that can switch THz wavelengths at high speed.

Generally, an ECLD selects a wavelength based on the angle of a mirror or diffraction grating. In our system, we used a DMD for this purpose [70]. In our setup, the light from the laser diode is diffracted by the grating and focused onto the DMD. Upon diffracted light input into the DMD, the oscillation wavelength can be selected by tilting the micromirrors in an appropriate manner. We used a ring cavity as the resonator to suppress spatial hole burning and achieve stable oscillation. Furthermore, because there is no amplified spontaneous emission from the laser diode, the ring cavity aspect of our system facilitates amplified spontaneous emission (ASE)-free, high signal-to-noise (S/N) ratio output. Thus, only a wavelength-selected beam can be output from the apparatus. For the DMD, we used a DLP4500NIR system (Texas Instruments, Inc.) controlled with an AJD-4500 controller (Ajile Light Industries) that allows for DMD operation up to 6 kHz. The tunability of this laser matches the speed of the DMD, confirming its proper operation as an injection seed for the is-TPG.

We measured the detection Stokes beam using an NIR camera as the THz wavelength was switched up to 17 wavelengths. Data for all wavelengths were obtained in one shot by adjusting the exposure time of the NIR camera according to the number of wavelengths. Figure 4(a) and 4(b) shows successful measurement of 10 and 17 wavelengths, respectively, during high-speed switching. As the number of wavelengths increased, the camera exposure time also increased, thus reducing the measurement rate. Although adjacent wavelengths overlapped among the 17 wavelengths, this overlap was not problematic during sample insertion because the image could be identified by machine learning (e.g., Fig. 4(c)).

Real-time measurement using the developed system was demonstrated with five-wavelength switching, as shown in Fig. 5. Five substances (maltose, Al(OH)$_3$, glucose, fructose, and lactose) in a cardboard box were spectrometrically measured by switching among the five frequencies indicated by red lines in Fig. 5. The detection Stokes beam near the absorption line weakened upon sample insertion, and spectroscopy at the video rate was achieved [71]. If a pump laser with a higher repetition rate becomes available, real-time spectroscopy with a larger number of wavelengths will be possible.

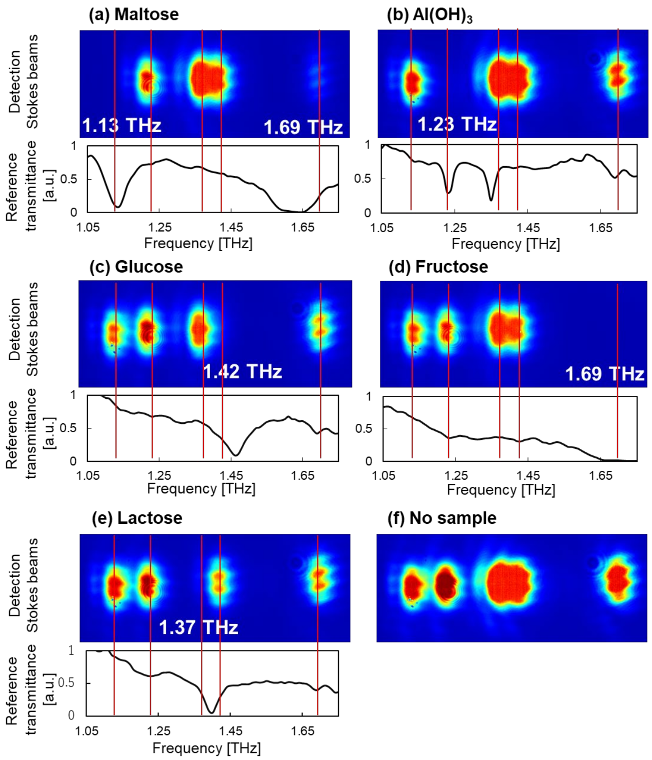

Fig. 5. Real-time measurement of each substance hidden in a cardboard box. (a–e) Detection Stokes beam with samples inserted into THz path (upper figures), along with reference spectra of each sample obtained by the is-TPG (lower figures) for (a) maltose, (b) Al(OH)$_3$, (c) glucose, (d) fructose, and (e) lactose. (f) Detection Stokes beam without samples.

VI. ONE-SHOT SPECTROSCOPY WITH A MULTI-WAVELENGTH IS-TPG

Next, we describe real-time spectroscopy with a multi-wavelength is-TPG. Although the fast wavelength switching described above can shorten the spectroscopy time, the measurement rate decreases as the number of wavelengths increases. If multiple wavelengths can be output simultaneously, real-time spectroscopy can be performed without decreasing the measurement rate; this capability is expected to expand the range of applications.

The general framework of the experimental system is equivalent to the system shown in Fig. 2(a); thus, the schematic diagram of Fig. 6 only shows parts that are important for multi-wavelength generation. The key step in the process comprises simultaneous input of the multi-wavelength seed beams into the LiNbO$_3$ crystal for multi-wavelength THz-wave generation. However, no commercially available continuous wave lasers can simultaneously generate multiple wavelengths near 1.07 µm. Therefore, we studied methos of multi-wavelength

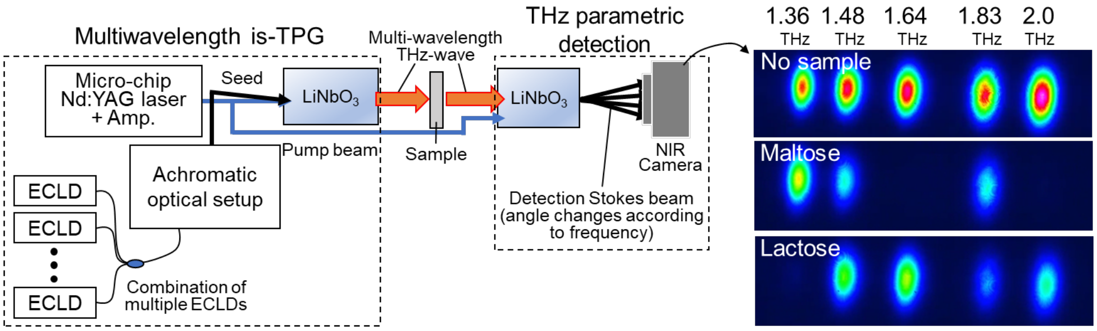

Fig. 6. Real-time spectrometer using a multi-wavelength is-TPG and changes in the detection Stokes beam during measurement of sugars.

generation via four-wave mixing inside of an amplifier [23] or through the use of an ECLD combined with a DMD [72].

Here, we report the experimental results of combining multiple ECLDs. Because spectral discrimination can be achieved when the number of wavelengths is equal to the number of absorption peaks of the test sample, light from five ECLDs was combined with a fiber coupler, amplified, and used as injection seeds in this context. In THz parametric detection of multi-wavelength THz-waves, the detection Stokes beam of each wavelength is emitted at a different angle according to the non-collinear phase-matching condition. Camera-based observations of these detection Stokes beams enable simultaneous collection of data regarding all wavelengths, as shown in Fig. 6 (right). Changes according to absorption peaks are obtained in a concurrent manner during sample insertion, indicating successful real-time spectroscopy measurement.

We investigated the possibility of using the described multi-wavelength spectroscopy system for THz tag measurement. A THz tag is a barcode that is read by THz-waves, even through packaging materials; thus, it differs from existing barcodes and tags. Various types of THz tags have been proposed [73–75].

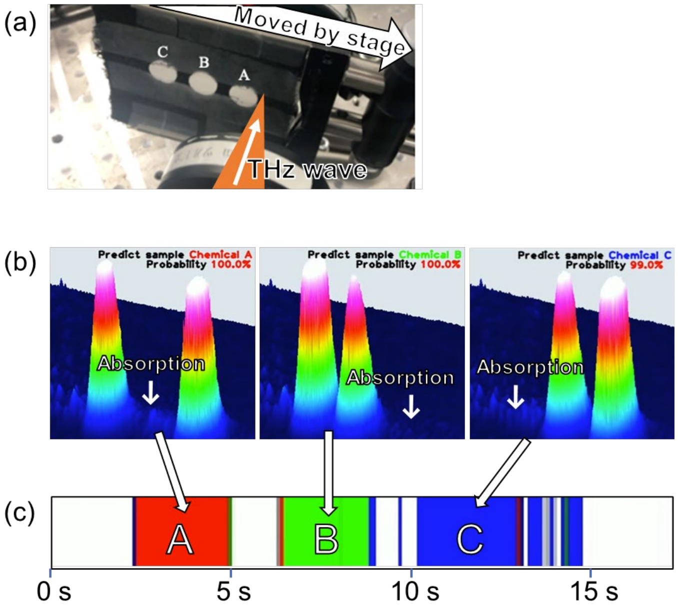

Fig. 7. Real-time identification of pellet sample. (a) View of measurement setup. (b) Detection Stokes beam for each pellet. (c) Results of real-time identification via machine learning.

Here, we offer a method for obtaining information from a sequence of pellets. In our approach, the detection Stokes beams from the multi-wavelength is-TPG are captured by a camera; the pellets are identified in real time by image recognition via machine learning. Ideally, many substances would be aligned to provide sufficient information in the form of a tag; here, three types of substances were measured sequentially as a simple analysis. We measured the pellets of aluminum hydroxide (chemical A), lactose (chemical B), and maltose (chemical C), as shown in Fig. 7(a). Pellets were identified through natural leather (thickness: 2.5 mm) with attenuation of approximately −40 dB at 1.2 THz. Using a uniaxial stage, we moved the pellets in the direction indicated by the arrow. Three frequencies were selected based on the absorption peak of each sample. As shown in Fig. 7(b), we collected screenshots from a video that showed the timing of measurement for each pellet. Figure 7(c) shows the results of real-time identification via machine learning. The pellets were identified in real time, along with the correct order of pellets; these findings demonstrated the utility of using machine learning for multi-wavelength measurements [60].

VII. MULTI-STAGE THZ PARAMETRIC DETECTION

Next, we describe a method for increasing the sensitivity of THz parametric detection. Our THz parametric detection method involves using nonlinear optical parametric wavelength conversion. This approach enables highly sensitive detection over a wide wavelength range, even at room temperature. To improve detection sensitivity, the parametric gain must be increased; this is usually achieved by increasing the pump beam intensity or crystal length [76]. However, the broadband Stokes beam (i.e., broadband noise) generated by spontaneous parametric down-conversion (i.e., optical or THz parametric generation) increases along with the parametric gain [22]. Therefore, the detection sensitivity decreases because the detection Stokes beam is masked by the broadband noise produced. Further improvements in detection sensitivity require enhancement of parametric gain and simultaneous elimination of broadband noise. Thus, we attempted to improve the detection sensitivity by separating the THz parametric detector into multiple stages using multiple LiNbO$_3$ crystals; we spatially eliminated broadband noise by using an iris between each stage.

Figure 8 shows the high-dynamic-range THz-wave measurement system involving a multi-stage THz parametric detector. In the conventional system, THz-waves were detected

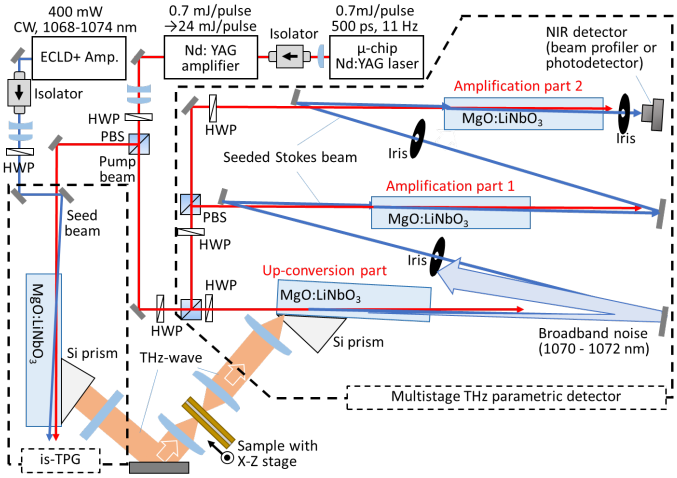

Fig. 8. High-dynamic-range THz measurement system involving multi-stage THz parametric detection and the is-TPG.

using a single crystal ("Up-conversion part" in the figure); the input THz-wave injected into the crystal would have been detected by an NIR detector after up-conversion to a detection Stokes beam. In the present system, this process is divided into two or three stages, as shown in Fig. 8. In the first stage, the THz-wave is converted into a detection Stokes beam using LiNbO$_3$ crystals. Because of the non-collinear phase-matching conditions, the generation angle of this detection Stokes beam depends on its frequency. Specifically, the generation angle of the detection Stokes beam generated by the single-frequency-input THz-wave differs from the generation angle of broadband noise; thus, the two waves can be separated in a spatial manner. Accordingly, only the detection Stokes beam is extracted by the iris; the beam is then injected into "Amplification part 1" and "Amplification part 2" (Fig. 8). Because only the detection Stokes beam is amplified in the latter stages, the gain can be increased during suppression of broadband noise.

For precise measurement of detection sensitivity, the input THz-wave energy must be correctly calibrated. Thus, the input THz-wave energy was calibrated while cross-checking using two pyroelectric detectors (THZ5I-MT-BNC; Gentec Electro-Optics; and THz 20; SLT Sensor und Lasertechnik). Then, the calibrated variable THz attenuator (three sets of TFA-4; Microtech Instruments, Inc) was inserted into the optical path of the input THz-wave to modify the energy. The minimum detection sensitivity and dynamic range were confirmed by the input THz-wave energy when the detection Stokes beam reached the noise level. When the THz-wave was blocked, the noise level was measured at each frequency. During this measurement, the intensity of the detection Stokes beam was determined by a beam profiler.

First, we attempted two-stage THz parametric detection using Amplification part 1. To determine the minimum detectable sensitivity, the intensity of the detection Stokes beam was measured upon alteration of the input THz-wave energy (frequency 1.05 THz). The results measured by the two-stage detector were compared with the results obtained by the conventional method using a single stage; here, "single stage" refers to the up-conversion part. As shown in Fig. 9(a), the minimum detectable sensitivity using a single stage was 1.3 aJ, consistent with the sensitivity reported by other groups; thus, the resulting value is regarded as the lower limit of the method using a single stage. Notably, the minimum detectable sensitivity using the multi-stage method was 130 zJ (= 10^{-21} J); this constituted an improvement of 10 dB, compared with the sensitivity achieved using a single stage.

Similar measurements were conducted for the other frequencies of 0.61, 0.79, 1.25, 1.50, and 2.0 THz. Figure 9(b) shows the frequency dependence of the minimum detectable energy. In this graph, the wavelength of the detection Stokes beam is shown on the upper axis, and the corresponding frequency of the THz-wave is shown on the lower axis. The minimum detectable sensitivity was optimized at 1.05 THz. In the low-frequency range, the minimum detectable sensitivity decreased because of the lower parametric gain. Conversely, in the high-frequency region, the minimum detectable sensitivity decreased as the frequency of the broadband noise overlapped the frequency of the detection Stokes beam. Based on these results, the minimum detectable sensitivity was optimized near 1 THz because of the balance between the parametric gain and noise.

The results were used to estimate the detection limit of THz photons. The energy per photon at 1.05 THz was approximately 0.6 zJ; a 130-zJ detection limit corresponds to approximately 217 photons. Furthermore, Fresnel losses occur at the interface

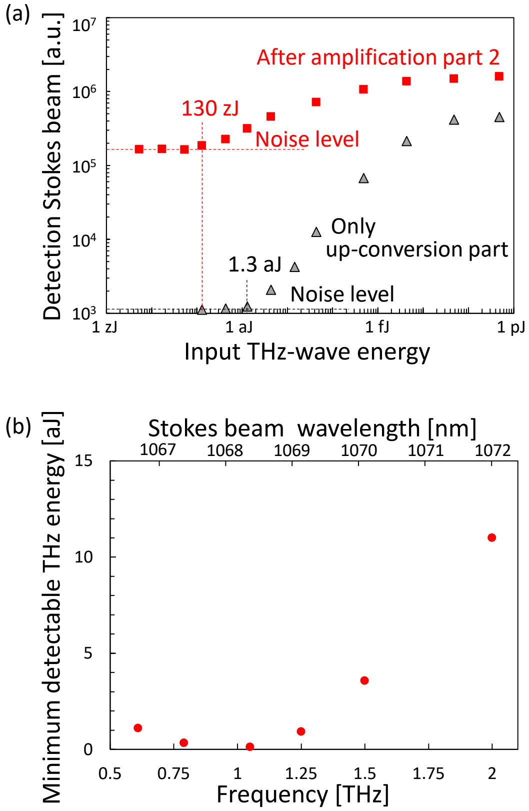

Fig. 9. (a) Input–output characteristics of two-stage THz-parametric detector at 1.05 THz. (b) Frequency dependence of minimum detectable energy. Wavelength of detection Stokes beam is shown on upper axis; corresponding frequency of THz-wave is shown on lower axis.

of the Si-prism and LiNbO$_3$, whereas absorption losses occur inside the LiNbO$_3$ crystal. Considering these losses, the detection limit was < 90 photons [25].

Although high-sensitivity detection was achieved, there were two problems. First, the change in the detection Stokes beam was smaller after amplification part 2 than after only the up-conversion part, as shown in Fig. 9(a) (i.e., linearity deteriorated). Second, the noise level of the detection Stokes beam was higher. These problems were caused by increasing the pump intensity and the gain during two-stage parametric detection to enhance the detection sensitivity. To solve these problems, we considered increasing the number of detection sections to three stages. Distribution of the necessary gain among three stages can facilitate reductions of the pump intensity and the gain at each crystal. These changes would improve detector linearity and suppress unnecessary broadband noise related to spontaneous parametric down-conversion.

The experimental results of the three-stage parametric amplification are described below; the schematic diagram of the experimental system is shown in Fig. 8. Only the signal beam was extracted by an iris from the detection Stokes beam amplified in the second stage, then injected into the LiNbO$_3$ crystal in the third stage. The THz-wave source was a pulse-synchronized is-TPG, with a frequency of 1.05 THz. The measured detection sensitivity is shown in Fig. 10. The calibrated THz-wave was used as the input, which decayed using a calibrated attenuator; the minimum detection sensitivity was set to the input level at which the detection Stokes beam change was lost. To determine the dynamic range of the measurement system combined with the is-TPG, the attenuation ratio for the maximum input was set to 0 dB, as shown at the top of the graph.

The detection sensitivity and dynamic range measurement results for two-stage detection, measured with an identical setup, are also shown in Fig. 10. The pump intensity was set to achieve the highest sensitivity in each setup. The change in the detection Stokes beam was larger in the three-stage configuration than in the two-stage configuration; additionally, the linearity improved in the three-stage configuration, and the noise level was reduced. However, there was no difference in the minimum detection sensitivity, and the sensitivity was very high (< 135 zJ). Notably, the differences between the two-stage configuration graphs in Figs. 9 and 10 are related to a change in alignment.

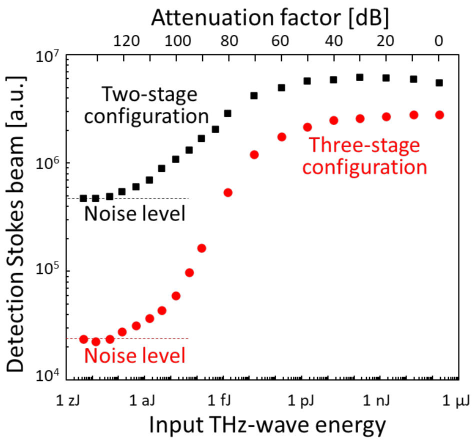

Fig. 10. Detection sensitivity measurement results for two- and three-stage THz parametric detection. To confirm the dynamic range as a measurement system combined with the is-TPG, we also showed the attenuation factor when maximum input is set to 0 dB.

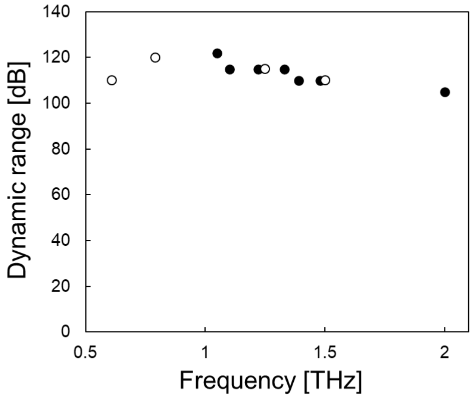

Fig. 11. Frequency dependences over the dynamic range of the system comprising three-stage THz parametric detection and the is-TPG. Frequencies measured with three-stage parametric detection are indicated by black circles, whereas frequencies measured with two-stage parametric detection are indicated by white circles.

Similar measurements were performed at other frequencies, and the frequency dependences of detection sensitivity were nearly equivalent to the dependence shown in Fig. 9(b). The frequency dependences over the dynamic range of the measurement system, combined with the is-TPG, are shown in Fig. 11; the results with two-stage detection are shown as white circles. A high dynamic range of more than 100 dB was obtained over a wide bandwidth, indicating that this system is ideal for measurement applications.

Next, we performed imaging through a packaging material using this system, considering its extremely high dynamic range. First, we report imaging at a single frequency of 1.05 THz, which has the highest dynamic range. The imaging targets were scissors and a key, as shown in Fig. 12(a). The scissors were

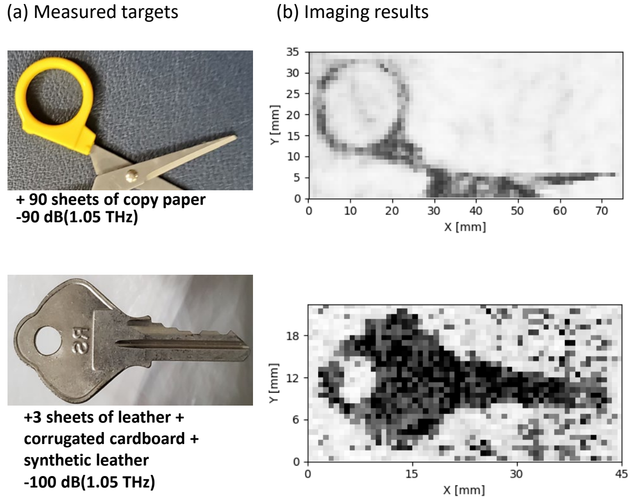
(a) Measured targets (b) Imaging results

Fig. 12. THz imaging through packaging materials with −90 dB to −100 dB attenuation: (a) metal targets and (b) imaging results.

hidden by 90 sheets of copy paper (−90 dB attenuation in total) and the key was hidden by 3 sheets of genuine leather + cardboard + synthetic leather (−100 dB attenuation in total). As shown in Fig. 12(b), the simple packaging materials of copy paper did not significantly affect the image quality; noise was slightly greater when imaging was conducted through multi-layered packaging materials with cardboard and leather. However, imaging was possible despite the use of complex packaging materials, demonstrating the strength and sensitivity of this measurement system for hidden objects.

Next, we describe the spectroscopic imaging using this system. The packaging materials used for spectroscopic imaging had a maximum attenuation of approximately 60 dB at 1.5 THz. Considering the absorption characteristics of substance themselves, it has been difficult to perform measurements with packaging materials that exhibit even higher attenuation. Here, we attempted spectroscopic imaging through a hidden object with higher attenuation, with the goal of exploiting the high dynamic range achieved in this study. As shown in Fig. 13(a), we prepared two types of packaging materials with nearly identical attenuation characteristics of −82 dB at 1.39 THz: 1) 55 sheets of copy paper; and 2) packaging materials comprising 4 sheets of cardboard, 2 sheets of cotton sheet, and 4 sheets of bubble wrap. The copy paper constitutes simple packaging materials with no structure; the composite packaging materials is a realistic arrangement with variable structure. Moreover, the copy paper has slightly lower attenuation in the low-frequency range. Four substance powders (a mixture of lactose and $Al(OH)_3$, maltose, lactose, and $Al(OH)_3$) were sealed in plastic bags at thicknesses of approximately 1 mm, then arranged in the order shown in Fig. 13(b). These substance have the absorption spectra shown in Fig. 13(c). Measurement frequencies (red lines) were selected according to the absorption peaks of each substance.

Here, we describe a method for analysis of spectroscopic images. Although we also reported a machine learning-based identification method in this paper, we used a conventional method (component spatial pattern analysis) [11, 53] for identification because only four measurement frequencies were used. This approach also allowed us to compare these results with spectroscopic imaging results obtained by using this conventional method in the p ast. In this identification method, the matrix [X] of the acquired image is the product of the reference spectrum [S] and the spatial pattern [C] of each substance:

$$[X] = [S][C] \,. \qquad (1)$$

Solving for [C] reveals the spatial distributions of the substances. Here, a large amount of training data is unnecessary, in contrast to the amount required for machine learning. The spatial pattern/distribution of each substance can be easily imaged for target identification because the pixel values are output as continuous values, rather than 0 or 1. However, this identification method requires the establishment of threshold values according to the type of packaging materials; thus, it should be used in a manner that is separate from the machine learning identification method, depending on the application.

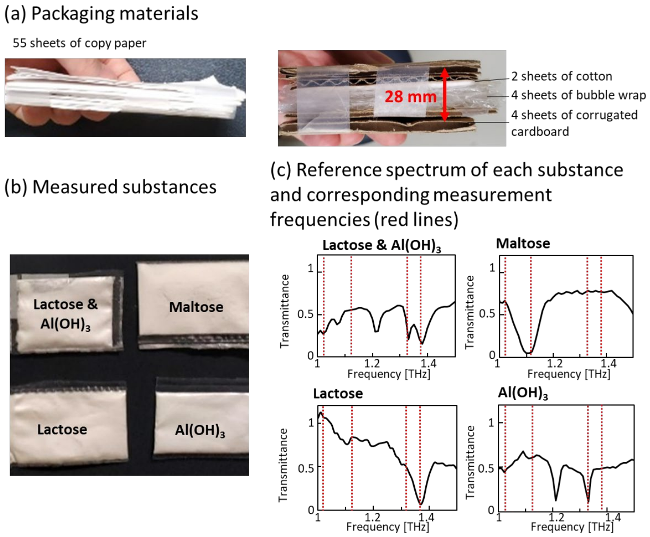

Fig. 13. Samples used for spectroscopic imaging. (a) The two packaging material types used, (b) measured substance and their arrangement, and (c) the absorption spectrum of each substance and the measurement frequencies selected (red lines).

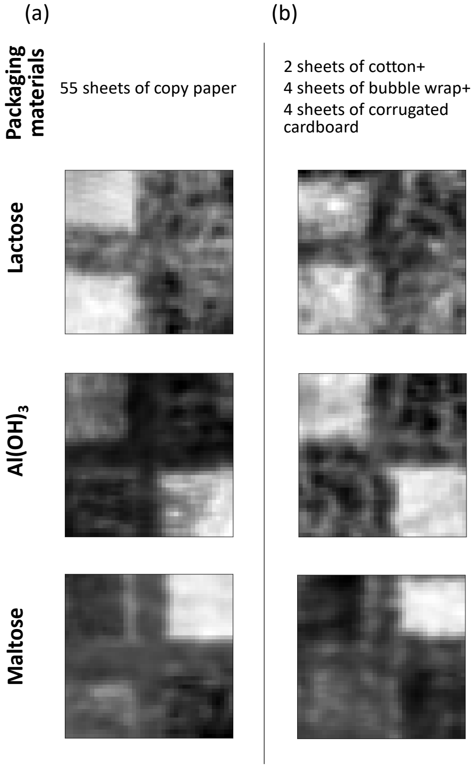

Fig. 14. Spectroscopic imaging results of sugars through packaging materials with attenuation of −82 dB: (a) > 55 sheets of copy paper and (b) composite packaging materials comprising cardboard and other materials.

Figure 14(a) and (b) shows the spectroscopic imaging results through the copy paper and the composite packaging materials, respectively; the results are normalized according to the maximum and minimum values in the images. Each sample is identified, and the substance mixture in the upper left is correctly identified in both "Lactose" and "$Al(OH)_3$" images. As shown in Fig. 14(a), the edges were little bit cleanly imaged through the copy paper packaging materials with low scattering; however, imaging was also possible with nearly identical accuracy through the composite packaging materials with high scattering (Fig. 14(b)). These results indicate that the is-TPG imaging system is appropriate for actual testing. As described above, the multi-stage detector achieves ultra-sensitive THz-wave detection, enabling measurement through packaging materials with extremely high attenuation (−100 dB for monochromatic imaging and −82 dB for spectroscopic imaging), which was difficult in previous studies.

VII. TPG NOISE LESS IS-TPG

Finally, as an attempt to further improve the performance of our THz-wave source, we will discuss the TPG noise less version of the is-TPG. As mentioned above, the is-TPG is an intense THz-wave source with a single longitudinal mode and wide tunability. However, the THz-wave output contains weak broadband noise ("broadband TPG noise") that is caused by spontaneous parametric down-conversion [77], although the power is approximately 1/10,000th of the power achieved with the injection-seeded THz-wave (i.e., "THz signal"). For example, in a measurement where the entire spectrum is attenuated, as in the imaging application shown in Fig. 11, broadband TPG noise is not problematic because it is concurrently attenuated. Conversely, during the measurement of samples in a pharmaceutical line, only some frequencies are strongly absorbed, and broadband TPG noise is not attenuated; this leads to deterioration of the S/N ratio. In such instances, TPG noise-less operation is necessary for the is-TPG. However, in the conventional system shown in Fig. 15(a), both the noise and signal are radiated into space by the Si coupler because the noise generation and signal generation locations are nearly identical.

In the reported method, broadband TPG noise was reduced by spatial extraction of the THz signal alone through an iris under non-colinear phase-matching conditions. This approach effectively removes broadband TPG noise [25, 27]; however, the iris position varies according to the frequency of the THz signal. Furthermore, the iris does not completely block broadband TPG noise in the vicinity of the THz signal.

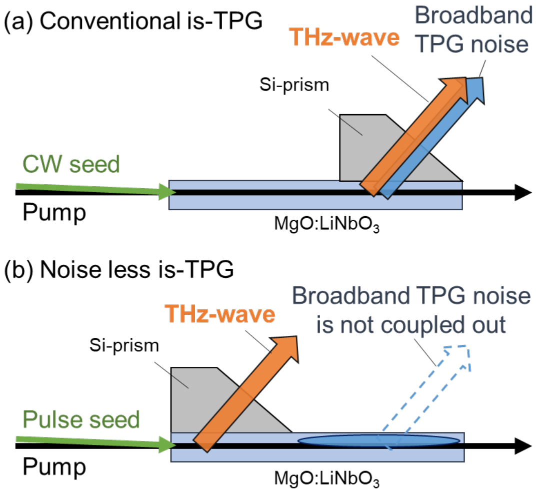

Fig. 15. (a) Conventional is-TPG involving weak continuous-wave injection-seeding. (b) TPG noise-less is-TPG involving high-power injection seeding.

Here, we achieved TPG noise-less THz-wave output from the is-TPG by focusing on the positions at which the injection-seeded pure THz signal and broadband TPG noise were generated. In a conventional is-TPG, the THz signal and broadband TPG noise are generated at nearly identical positions because of the weak seed beam, as shown in Fig. 15(a). In contrast, when using a pulsed high-power seed beam, we found that the THz signal was generated at a position toward the front of the crystal [Fig. 15(b)]. Because broadband TPG noise was solely generated by the pump beam, such noise was generated (as in a previous experiment) from the rear of the crystal, regardless of whether seed beam power was increased. Therefore, we were able to specifically extract the THz signal from the $LiNbO_3$ crystal by adjusting the position of the Si-prism.

To confirm TPG noise-less THz-wave output, we used a notch filter to suppress the THz signal alone; this revealed whether any weak TPG noise remained at the bottom. The notch filter was created by mixing 150 mg of lactose (with a sharp absorption line at 1.37 THz) and polyethylene, followed by pelleting. The filter attenuated a 1.37-THz signal by −55 dB. We set the pure THz-wave frequency to 1.37 THz, then inserted a notch filter at the focal point of the THz-wave to attenuate only the THz signal.

Figure 16 shows the THz spectra of the conventional and TPG noise-less is-TPGs obtained by the THz parametric detector. The blue and orange lines are THz spectra with and without the notch filter, respectively. The inset of Fig. 16(a) shows that broadband TPG noise was evident around the THz signal of the conventional is-TPG. In contrast, as shown in the inset of Fig. 16(b), no noise was observed when using the pulse-seeded is-TPG.

Moreover, when the THz signal was reduced to −95 dB by a higher concentration of lactose pellets, no broadband TPG noise

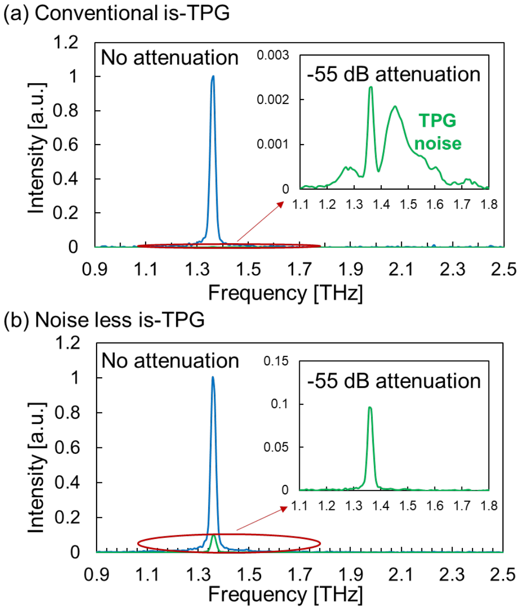

Fig. 16. THz spectra of (a) conventional is-TPG and (b) TPG noise-less is-TPG. Insets show spectra derived after insertion of a notch filter (i.e., lactose filter) with attenuation of −55 dB at 1.37 THz.

(a) Conventional is-TPG

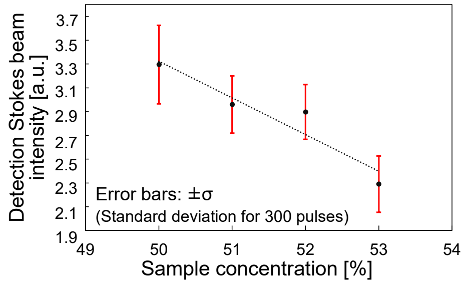

(b) Noise less is-TPG

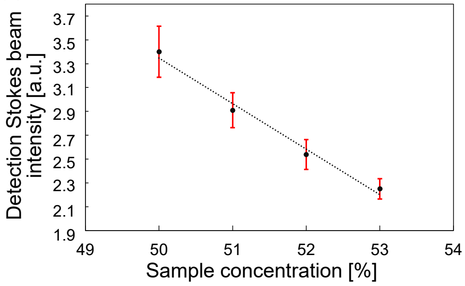

Fig. 17. Example of quantitative measurement of a high-concentration substance pellet with strong attenuation only at a specific frequency. Change in detection Stokes beam intensity of lactose pellets with concentration variations of 1% when measured with (a) conventional is-TPG and (b) TPG noise-less is-TPG.

was observed. Thus, the S/N ratio of 55 dB for the conventional is-TPG was improved to > 95 dB for the pulse-seeded is-TPG [78].

Assuming the measurement of highly concentrated substance samples that are strongly attenuated only at a specific frequency, consistent with requirements in pharmaceutical and other fields, quantitative measurements of substance pellets were performed using the TPG noise-less is-TPG described above. The detection Stokes beam intensity was observed when the concentration of lactose pellets was modified from 50% to 53% in increments of 1%; we examined whether the difference in concentration could be correctly determined. Notably, attenuation of the 50% pellet approached −60 dB at 1.3 THz; this measurement utilizes the high dynamic range of the is-TPG. When measured with the conventional is-TPG shown in Fig. 17(a), the error bars (representing standard deviation of 300 pulses) overlap each other. In contrast, using the TPG noise-less is-TPG shown in Fig. 17(b), the error bars are smaller, indicating the ability to determine each concentration. These findings demonstrate the suitability of using the TPG noise-less is-TPG with a high S/N ratio for measurements of substances with high concentration and purity, as required in pharmaceutical and other fields.

VIII. CONCLUSION

In summary, we have described high-performance spectroscopy systems and nondestructive testing techniques using an is-TPG and THz parametric detection; the performances of these methods have been dramatically improved by recent technological innovations. First, we described the introduction of machine learning into spectroscopy systems. This approach allows highly accurate identification of substances, regardless of the attenuation of measured samples. Furthermore, weak signals buried in noise can be identified with high accuracy; spectroscopic imaging through thick packaging materials is also possible. Next, we discussed high-speed wavelength tuning. We fabricated an injection seed laser with a DMD in the wavelength tuning mechanism, which enabled high-speed switching of arbitrary wavelengths to match sample absorption peaks; this approach dramatically improved the speed of spectroscopic measurement. Furthermore, simultaneous generation of multiple wavelengths was successfully achieved, enabling real-time spectroscopic analysis of substances. The camera-measured detection Stokes beam images were recognized by machine learning, enabling instantaneous sample identification. Improvements in THz-wave detection technologies were also discussed. Multi-stage THz parametric detection improves the parametric gain, while eliminating broadband noise. Ultra-weak THz-wave detection of < 1 aJ/pulse was achieved; the dynamic range of the spectrometer system combined with the is-TPG reached more than 120 dB. This enabled the imaging of a target hidden in thick packaging materials with −100 dB attenuation. Finally, we described the TPG noise-less is-TPG. Pulsing of the injection seed allowed the positions of signal generation and noise generation to be separated, thereby producing TPG noise-less operation. In addition to the new technologies described in this report, we have constructe d a high-efficiency is-TPG using a flat pump beam for further cost reduction, as well as a THz parametric amplifier with extremely high amplification. In future work, we will continue to explore practical applications of THz-wave inspection technology.

ACKNOWLEDGMENT

Authors would like to thank Dr. S. Hayashi of NICT; Dr. H. Minamide, Dr. K. Nawata and Y. Takida of Riken; Prof. T. Taira of IMS for the useful discussions; Mr. K. Nagase, Mr. T. Horiuchi, Ms. H. Sakai, Mr. H. Kanai, and Mr. R. Mitsuhashi of Nagoya University for assistance in the experiments.

REFERENCES

[1] L. Xie, Y. Yao, and Y. Ying, "The Application of Terahertz Spectroscopy to Protein Detection: A Review," *Appl. Spectrosc. Rev.*, vol. 49, no. 6, pp. 448–461, Aug. 2014, doi: 10.1080/05704928.2013.847845.

[2] L. Afsah-Hejri, P. Hajeb, P. Ara, and R. J. Ehsani, "A comprehensive review on food applications of terahertz spectroscopy and imaging," *Compr. Rev. Food Sci. Food Saf.*, vol. 18, no. 5, pp. 1563–1621, Aug. 2019. doi: 10.1111/1541-4337.12490

[3] M. O. AlNabooda, R. M. Shubair, N. R. Rishani, and G. Aldabbagh, "Terahertz spectroscopy and imaging for the detection and identification of Illicit drugs," in *Proc. 2017 SENSET*, Sep. 2017, pp. 1–4.

[4] C. Du, X. Zhang, and Z. Zhang, "Quantitative analysis of ternary isomer mixtures of saccharide by terahertz time domain spectroscopy combined with chemometrics," *Vib. Spectrosc.*, vol. 100, pp. 64–70, Jan. 2019, doi: 10.1016/j.vibspec.2018.11.003.

[5] S. G. Carter *et al.*, *Terahertz Spectroscopy Principles and Applications*. Boca Raton: CRC Press, 2017. doi: 10.1201/9781420007701.

[6] H. Zhang, Z. Li, T. Chen, and J. Liu, "Discrimination of traditional herbal medicines based on terahertz spectroscopy," *Optik*, vol. 138, pp. 95–102, Jun. 2017, doi: 10.1016/j.ijleo.2017.03.037.

[7] M. Massaouti, C. Daskalaki, A. Gorodetsky, A. D. Koulouklidis, and S. Tzortzakis, "Detection of Harmful Residues in Honey Using Terahertz Time-Domain Spectroscopy," *Appl. Spectrosc.*, vol. 67, no. 11, pp. 1264–1269, Nov. 2013, doi: 10.1366/13-07111.

[8] M. Tonouchi, “Cutting-edge terahertz technology,” *Nat. Photonics*, vol. 1, no. 2, pp. 97–105, 2007, doi: 10.1038/nphoton.2007.3.

[9] W. Yi *et al.*, “Broadband terahertz spectroscopy of amino acids,” *Instrum. Sci. Technol.*, vol. 45, no. 4, pp. 423–439, Jul. 2017, doi: 10.1080/10739149.2016.1270961.

[10] K. B. Cooper, R. J. Dengler, N. Llombart, B. Thomas, G. Chattopadhyay, and P. H. Siegel, “THz Imaging Radar for Standoff Personnel Screening,” *IEEE Trans. Terahertz Sci. Technol.*, vol. 1, no. 1, pp. 169–182, Sep. 2011, doi: 10.1109/TTHZ.2011.2159556.

[11] K. Kawase, Y. Ogawa, Y. Watanabe, and H. Inoue, “Non-destructive terahertz imaging of illicit drugs using spectral fingerprints,” *Opt. express*, vol. 11, no. 20, pp. 2549–2554, 2003, doi: 10.1364/OE.11.002549.

[12] H. Minamide, “Development of High-Power Terahertz-Wave Sources for Finding Novel Applications,” *IEEE Trans. Terahertz Sci. Technol.*, vol. 5, no. 6, pp. 1104–1109, Nov. 2015.

[13] D. Shrekenhamer, C. M. Watts, and W. J. Padilla, “Terahertz single pixel imaging with an optically controlled dynamic spatial light modulator,” *Opt. Express*, vol. 21, no. 10, pp. 12507–12518, May 2013, doi: 10.1364/OE.21.012507.

[14] E. Öjefors, A. Lisauskas, D. Glaab, H. G. Roskos, and U. R. Pfeiffer, “Terahertz Imaging Detectors in CMOS Technology,” *J. Infrared Millim. Terahertz Waves*, vol. 30, no. 12, pp. 1269–1280, Dec. 2009, doi: 10.1007/s10762-009-9569-4.

[15] Ning Li *et al.*, “Non-destructive inspections of illicit drugs in envelope using terahertz time-domain spectroscopy,” in *Proc. SPIE*, Oct. 2006, vol. 6047, p. 60472Y. doi: 10.1117/12.710671.

[16] A. Luukanen, R. Appleby, M. Kemp, and N. Salmon, “Millimeter-Wave and Terahertz Imaging in Security Applications,” in *Terahertz Spectroscopy and Imaging*, K.-E. Peiponen, A. Zeitler, and M. Kuwata-Gonokami, Eds. Berlin, Heidelberg: Springer Berlin Heidelberg, 2013, pp. 491–520. doi: 10.1007/978-3-642-29564-5_19.

[17] B. C. Johnson, H. E. Puthoff, J. SooHoo, and S. S. Sussman, “POWER AND LINEWIDTH OF TUNABLE STIMULATED FAR-INFRARED EMISSION IN LiNbO3,” *Appl. Phys. Lett.*, vol. 18, no. 5, pp. 181–183, Mar. 1971, doi: 10.1063/1.1653616.

[18] J. M. Yarborough, S. S. Sussman, H. E. Purhoff, R. H. Pantell, and B. C. Johnson, “EFFICIENT, TUNABLE OPTICAL EMISSION FROM LiNbO3 WITHOUT A RESONATOR,” *Appl. Phys. Lett.*, vol. 15, no. 3, pp. 102–105, Aug. 1969, doi: 10.1063/1.1652910.

[19] K. Kawase, M. Sato, T. Taniuchi, and H. Ito, “Coherent tunable THz-wave generation from $LiNbO_3$ with monolithic grating coupler,” *Appl. Phys. Lett.*, vol. 68, no. 18, pp. 2483–2485, 1996, doi: 10.1063/1.115828.

[20] K. Kawase, H. Minamide, K. Imai, J. Shikata, and H. Ito, “Injection-seeded terahertz-wave parametric generator with wide tunability,” *Appl. Phys. Lett.*, vol. 80, no. 2, pp. 195–197, Jan. 2002, doi: 10.1063/1.1429299.

[21] H. Sakai, H. Kan, and T. Taira, “>1 MW peak power single-mode high-brightness passively Q-switched Nd^{3+}:YAG microchip laser,” *Opt. Express*, vol. 16, no. 24, pp. 19891–19899, Nov. 2008, doi: 10.1364/OE.16.019891.

[22] S. Hayashi, K. Nawata, T. Taira, J. Shikata, K. Kawase, and H. Minamide, “Ultrabright continuously tunable terahertz-wave generation at room temperature,” *Sci. Rep.*, vol. 4, no. 1, Art. no. 1, Jun. 2014, doi: 10.1038/srep05045.

[23] K. Murate, S. Hayashi, and K. Kawase, “Multiwavelength terahertz-wave parametric generator for one-pulse spectroscopy,” *Appl. Phys. Express*, vol. 10, no. 3, p. 032401, 2017, doi: 10.7567/APEX.10.032401.

[24] R. Guo, S. Ohno, H. Minamide, T. Ikari, and H. Ito, “Highly sensitive coherent detection of terahertz waves at room temperature using a parametric process,” *Appl. Phys. Lett.*, vol. 93, no. 2, p. 021106, Jul. 2008, doi: 10.1063/1.2953452.

[25] H. Sakai, K. Kawase, and K. Murate, “Highly sensitive multi-stage terahertz parametric detector,” *Opt. Lett.*, vol. 45, no. 14, pp. 3905–3908, 2020, doi: 10.1364/OL.394975.

[26] Y. Taira *et al.*, “A Terahertz Wave Parametric Amplifier With a Gain of 55 dB,” *IEEE Trans. Terahertz Sci. Technol.*, vol. 4, no. 6, pp. 753–755, Nov. 2014, doi: 10.1109/TTHZ.2014.2355179.

[27] K. Murate, H. Sakai, and K. Kawase, “Six-Billion-Fold Amplification via a Two-Stage Terahertz Parametric Amplifier,” *IEEE Trans. Terahertz Sci. Technol.*, vol. 10, no. 2, pp. 200–203, Mar. 2020, doi: 10.1109/TTHZ.2020.2964832.

[28] K. Nawata, Y. Tokizane, Y. Takida, and H. Minamide, “Tunable backward terahertz-wave parametric oscillation,” *Sci. Rep.*, vol. 9, no. 1, pp. 1–6, 2019, doi: 10.1038/s41598-018-37068-7.

[29] Y. Takida, K. Nawata, and H. Minamide, “Injection-seeded backward terahertz-wave parametric oscillator,” *APL Photonics*, vol. 5, no. 6, p. 061301, Jun. 2020, doi: 10.1063/5.0007306.

[30] D. Molter, M. Theuer, and R. Beigang, “Nanosecond terahertz optical parametric oscillator with a novel quasi phase matching scheme in lithium niobate,” *Opt. Express*, vol. 17, no. 8, pp. 6623-6628, Apr. 2009, doi: 10.1364/OE.17.006623.

[31] K. Chen *et al.*, “Continuously Tunable and Energy-Enhanced Injection Pulse-Seeded Terahertz Parametric Generator Based on KTP Crystal,” *ACS Photonics*, vol. 8, no. 11, pp. 3141–3149, Nov. 2021, doi: 10.1021/acsphotonics.1c00284.

[32] Y. Wang *et al.*, “Highly sensitive multi-stage terahertz parametric upconversion detection based on a $KTiOPO_4$ crystal,” *Opt. Lett.*, vol. 47, no. 22, pp. 5853–5856, Nov. 2022, doi: 10.1364/OL.473955.

[33] M.-H. Wu, W.-C. Tsai, Y.-C. Chiu, and Y.-C. Huang, “Generation of ~ 100 kW narrow-line far-infrared radiation from a KTP off-axis THz parametric oscillator,” *Optica*, vol. 6, no. 6, pp. 723–730, Jun. 2019, doi: 10.1364/OPTICA.6.000723.

[34] R. Li, Y. Zheng, D. J. Spence, H. M. Pask, and A. J. Lee, “Intracavity THz Polariton Source Using a Shallow-Bounce Configuration,” *IEEE Trans. Terahertz Sci. Technol.*, vol. 9, no. 3, Art. no. 3, May 2019, doi: 10.1109/TTHZ.2019.2900586.

[35] T. A. Ortega, H. M. Pask, D. J. Spence, and A. J. Lee, “THz polariton laser using an intracavity Mg:$LiNbO_3$ crystal with protective Teflon coating,” *Opt. Express, OE*, vol. 25, no. 4, Art. no. 4, Feb. 2017, doi: 10.1364/OE.25.003991.

[36] Y. Moriguchi *et al.*, “High-average and high-peak output-power terahertz-wave generation by optical parametric down-conversion in MgO: $LiNbO_3$,” *Appl. Phys. Lett.*, vol. 113, no. 12, p. 121103, 2018, doi: 10.1063/1.5046126.

[37] Y. Wada, T. Satoh, Y. Higashi, and Y. Urata, “Compact Tunable Narrowband Terahertz-Wave Source Based on Difference Frequency Generation Pumped by Dual Fiber Lasers in MgO:LiNbO3,” *J Infrared Milli Terahz Waves*, vol. 38, no. 12, Art. no. 12, Dec. 2017, doi: 10.1007/s10762-017-0437-3.

[38] W. Li *et al.*, “Cascaded effect in a high-peak-power terahertz-wave parametric generator,” *Opt. Lett., OL*, vol. 47, no. 1, pp. 178–181, Jan. 2022, doi: 10.1364/OL.441786.

[39] S. W. Jolly *et al.*, “Spectral phase control of interfering chirped pulses for high-energy narrowband terahertz generation,” *Nat. Comm.*, vol. 10, no. 1, p. 2591, Jun. 2019, doi: 10.1038/s41467-019-10657-4.

[40] T. Pfeiffer, M. Kutas, B. Haase, D. Molter, and G. von Freymann, “Terahertz detection by upconversion to the near-infrared using picosecond pulses,” *Opt. Express*, vol. 28, no. 20, pp. 29419–29429, Sep. 2020, doi: 10.1364/OE.397839.

[41] W. Kong, Z. Li, Q. Yan, M. Zou, X. Zhou, and Y. Qin, “Theoretical and experimental study on the enhancement of seed injection in terahertz-wave generation,” *JOSA B*, vol. 37, no. 8, pp. 2479–2484, 2020, doi: 10.1364/JOSAB.393661.

[42] W. Kong, Q. Yan, Z. Li, M. Zou, X. Zhou, and Y. Qin, “Nonlinear optical up-conversion in terahertz parametric process: simulation and experiment,” *IEEE Trans. Terahertz Sci. Technol.*, 2021, doi: 10.1109/TTHZ.2021.3054181.

[43] K. Murate and K. Kawase, “Perspective: Terahertz wave parametric generator and its applications,” *J. Appl. Phys*, vol. 124, no. 16, p. 160901, 2018, doi: 10.1063/1.5050079.

[44] C. H. Henry and C. G. B. Garrett, “Theory of Parametric Gain near a Lattice Resonance,” *Phys. Rev.*, vol. 171, no. 3, pp. 1058–1064, Jul. 1968, doi: 10.1103/PhysRev.171.1058.

[45] J. Shikata, K. Kawase, M. Sato, T. Taniuchi, and H. Ito, “Characteristics of coherent terahertz wave generation from $LiNbO_3$ optical parametric oscillator,” *Electron. Commun. Jpn.*, vol. 82, no. 5, pp. 46–53, May 1999, doi: 10.1002/(SICI)1520-6432(199905)82:5<46::AID-ECJB6>3.0.CO;2-S.

[46] M. V. Hobden and J. Warner, “The temperature dependence of the refractive indices of pure lithium niobate,” *Phys. Lett.*, vol. 22, no. 3, pp. 243–244, Aug. 1966, doi: 10.1016/0031-9163(66)90591-9.

[47] D. R. Bosomworth, “THE FAR INFRARED OPTICAL PROPERTIES OF LiNbO3,” *Appl. Phys. Lett.*, vol. 9, no. 9, pp. 330–331, Nov. 1966, doi: 10.1063/1.1754772.

[48] K. Imai, K. Kawase, H. Minamide, and H. Ito, “Achromatically injection-seeded terahertz-wave parametric generator,” *Opt. Lett.*, vol. 27, no. 24, pp. 2173–2175, 2002, doi: 10.1364/OL.27.002173.

[49] K. Murate, S. Hayashi, and K. Kawase, “Expansion of the tuning range of injection-seeded terahertz-wave parametric generator up to 5 THz,” *Appl. Phys. Express*, vol. 9, no. 8, p. 082401, 2016, doi: 10.7567/APEX.9.082401.

[50] S. Hayashi, K. Nawata, Y. Takida, Y. Tokizane, K. Kawase, and H. Minamide, “High-Brightness Continuously Tunable Narrowband Subterahertz Wave Generation,” *IEEE Trans. Terahertz Sci. Technol.*, vol. 6, no. 6, Art. no. 6, Nov. 2016, doi: 10.1109/TTHZ.2016.2611939.

[51] K. Nawata *et al.*, “Effective terahertz wave parametric generation depending on the pump pulse width using a LiNbO$_3$ crystal,” *IEEE Trans. Terahertz Sci. Technol.*, vol. 7, no. 5, pp. 617–620, 2017, doi: 10.1109/TTHZ.2017.2725479.

[52] K. Murate *et al.*, “A High Dynamic Range and Spectrally Flat Terahertz Spectrometer Based on Optical Parametric Processes in LiNbO$_3$,” *IEEE Trans. Terahertz Sci. Technol.*, vol. 4, no. 4, Art. no. 4, Jul. 2014, doi: 10.1109/TTHZ.2014.2326298.

[53] M. Kato, S. R. Tripathi, K. Murate, K. Imayama, and K. Kawase, “Non-destructive drug inspection in covering materials using a terahertz spectral imaging system with injection-seeded terahertz parametric generation and detection,” *Opt. Express*, vol. 24, no. 6, pp. 6425–6432, 2016, doi: 10.1364/OE.24.006425.

[54] S. R. Tripathi, Y. Sugiyama, K. Murate, K. Imayama, and K. Kawase, “Terahertz wave three-dimensional computed tomography based on injection-seeded terahertz wave parametric emitter and detector,” *Opt. Express,* vol. 24, no. 6, pp. 6433–6440, Mar. 2016, doi: 10.1364/OE.24.006433.

[55] D. S. Bulgarevich, M. Talara, M. Tani, and M. Watanabe, “Machine learning for pattern and waveform recognitions in terahertz image data,” *Sci. Rep.*, vol. 11, no. 1, p. 1251, Jan. 2021, doi: 10.1038/s41598-020-80761-9.

[56] H. Ge, Y. Jiang, Z. Xu, F. Lian, Y. Zhang, and S. Xia, “Identification of wheat quality using THz spectrum,” *Opt. Express*, vol. 22, no. 10, pp. 12533–12544, May 2014, doi: 10.1364/OE.22.012533.

[57] B. Sun, X. Bai, J. Liu, and J. Yao, “Investigation of a terahertz-wave parametric oscillator using LiTaO3 with the pump-wavelength tuning method,” *Laser Phys.*, vol. 24, no. 3, p. 035402, Feb. 2014, doi: 10.1088/1054-660X/24/3/035402.

[58] C. Cao, Z. Zhang, X. Zhao, and T. Zhang, “Terahertz spectroscopy and machine learning algorithm for non-destructive evaluation of protein conformation,” *Opt. Quantum Electron.,* vol. 52, no. 4, p. 225, Apr. 2020, doi: 10.1007/s11082-020-02345-1.

[59] W. Liu *et al.*, “Automatic recognition of breast invasive ductal carcinoma based on terahertz spectroscopy with wavelet packet transform and machine learning,” *Biomed. Opt. Express*, vol. 11, no. 2, pp. 971–981, Feb. 2020, doi: 10.1364/BOE.381623.

[60] R. Mitsuhashi, K. Murate, S. Niijima, T. Horiuchi, and K. Kawase, “Terahertz tag identifiable through shielding materials using machine learning,” *Opt. Express*, vol. 28, no. 3, pp. 3517–3527, Feb. 2020, doi: 10.1364/OE.384195.

[61] Y. Jiang *et al.*, “Machine Learning and Application in Terahertz Technology: A Review on Achievements and Future Challenges,” *IEEE Access*, vol. 10, pp. 53761–53776, 2022, doi: 10.1109/ACCESS.2022.3174595.

[62] K. Murate, H. Kanai, and K. Kawase, “Application of Machine Learning to Terahertz Spectroscopic Imaging of Reagents Hidden By Thick Shielding Materials,” *IEEE Trans. Terahertz Sci. Technol.*, vol. 11, no. 6, pp. 620–625, Nov. 2021, doi: 10.1109/TTHZ.2021.3094128.

[63] C. J. C. Burges, “A Tutorial on Support Vector Machines for Pattern Recognition,” *Data Mining and Knowledge Discovery*, vol. 2, no. 2, Art. no. 2, Jun. 1998, doi: 10.1023/A:1009715923555.

[64] C. Bishop, *Pattern Recognition and Machine Learning*. New York: Springer-Verlag, 2006. Accessed: Oct. 21, 2020. [Online]. Available: https://www.springer.com/jp/book/9780387310732

[65] S. A. Dudani, “The Distance-Weighted k-Nearest-Neighbor Rule,” *IEEE Trans. Syst. Man Cybern. Syst.*, vol. SMC-6, no. 4, Art. no. 4, Apr. 1976, doi: 10.1109/TSMC.1976.5408784.

[66] L. Breiman, “Random Forests,” *Machine Learning*, vol. 45, no. 1, Art. no. 1, Oct. 2001, doi: 10.1023/A:1010933404324.

[67] Y. Moriguchi *et al.*, “Frequency-agile injection-seeded terahertz-wave parametric generation,” *Opt. Lett.*, vol. 45, no. 1, pp. 77–80, 2020.

[68] N. A. Riza and M. J. Mughal, “Broadband optical equalizer using fault-tolerant digital micromirrors,” *Opt. Express*, vol. 11, no. 13, pp. 1559–1565, Jun. 2003, doi: 10.1364/OE.11.001559.

[69] Mikhail A. Gutin and James Castracane, “Fast tunable diode laser with digital control and multiple line selection,” in *Proc. SPIE*, Apr. 1999, vol. 3626, pp. 53–60. doi: 10.1117/12.345415.

[70] S. Mine, K. Kawase, and K. Murate, “High-power ASE-free fast wavelength-switchable external cavity diode laser,” *Appl. Opt.,* vol. 60, no. 7, pp. 1953–1957, Mar. 2021, doi: 10.1364/AO.416033.

[71] S. Mine, K. Kawase, and K. Murate, “Real-time wide dynamic range spectrometer using a rapidly wavelength-switchable terahertz parametric source,” *Opt. Lett.*, vol. 46, no. 11, pp. 2618–2621, 2021, doi: 10.1364/OL.423985.

[72] S. Mine, K. Kawase, and K. Murate, “Multi-Wavelength Terahertz Parametric Generator Using a Seed Laser Based on Four-Wave Mixing,” *Photonics*, vol. 9, no. 4, 2022, doi: 10.3390/photonics9040258.

[73] M. Hamdi, F. Garet, L. Duvillaret, P. Martinez, and G. Eymin Petot Tourtollet, “Identification tag in the terahertz frequency domain using low-cost and tunable refractive index materials,” *Ann. Telecommun.*, vol. 68, no. 7, pp. 415–424, Aug. 2013, doi: 10.1007/s12243-013-0374-7.

[74] Y. Kujime, M. Fujita, and T. Nagatsuma, “Terahertz Tag Using Photonic-Crystal Slabs,” *J. Light. Technol.*, vol. 36, no. 19, pp. 4386–4392, Oct. 2018, doi: 10.1109/JLT.2018.2825464.

[75] Y. Amarasinghe, H. Guerboukha, Y. Shiri, and D. M. Mittleman, “Bar code reader for the THz region,” *Opt. Express, OE*, vol. 29, no. 13, pp. 20240–20249, Jun. 2021, doi: 10.1364/OE.428547.

[76] Y. Takida *et al.*, “Terahertz-wave parametric gain of stimulated polariton scattering,” *Phys. Rev. A*, vol. 93, no. 4, p. 043836, Apr. 2016, doi: 10.1103/PhysRevA.93.043836.

[77] G. K. Kitaeva, V. V. Kornienko, A. A. Leontyev, and A. V. Shepelev, “Generation of optical signal and terahertz idler photons by spontaneous parametric down-conversion,” *Phys. Rev. A*, vol. 98, no. 6, p. 063844, 2018, doi: 10.1103/PhysRevA.98.063844.

[78] S. Mine, K. Kawase, and K. Murate, “Noise-free terahertz-wave parametric generator,” *Opt. Lett.*, vol. 47, no. 5, pp. 1113–1116, 2022, doi: 10.1364/OL.448636.

Kosuke Murate (Member, IEEE) received B.S., M.S. and Ph.D. degrees from Nagoya University, Japan in 2013, 2015, and 2018, respectively. Now he is working as an assistant professor in the Department of Electronics, Graduate school of Engineering, Nagoya University since 2018. He received Ikushi prize from Japan Society for the Promotion of Science in 2018.

Sota Mine received the B.S. and M.S. degrees from Nagoya University in 2020 and 2022, and now he is a Ph.D course student in Department of Electronics, Graduate school of Engineering, Nagoya University in Japan.

Kodo Kawase received the B.S. degree from Kyoto Univ. in 1989, and the Ph. D degrees from Tohoku Univ. in 1996. He became a team leader of RIKEN in 2001. He became a Professor of Nagoya University in 2005. He received the 2005 Young Scientists’ Prize by the Minister of Education.